

A Machine Learning-Driven Solution for Denoising Inertial Confinement Fusion Images

Asya Y. Akkus, Bradley T. Wolfe, Pinghan Chu, Chengkun Huang, Chris S. Campbell, Mariana Alvarado Alvarez, Petr Volegov, David Fittinghoff, Robert Reinovsky, Zhehui Wang

Abstract—Neutron imaging is essential for diagnosing and optimizing inertial confinement fusion implosions at the National Ignition Facility. Due to the required 10- μm resolution, however, neutron image require image reconstruction using iterative algorithms. For low-yield sources, the images may be degraded by various types of noise. Gaussian and Poisson noise often coexist within one image, obscuring fine details and blurring the edges where the source information is encoded. Traditional denoising techniques, such as filtering and thresholding, can inadvertently alter critical features or reshape the noise statistics, potentially impacting the ultimate fidelity of the iterative image reconstruction pipeline. However, recent advances in synthetic data production and machine learning have opened new opportunities to address these challenges. In this study, we present an unsupervised autoencoder with a Cohen-Daubechies-Feauveau (CDF 97) wavelet transform in the latent space, designed to suppress for mixed Gaussian-Poisson noise while preserving essential image features. The network successfully denoises neutron imaging data. Benchmarking against both simulated and experimental NIF datasets demonstrates that our approach achieves lower reconstruction error and superior edge preservation compared to conventional filtering methods such as Block-matching and 3D filtering (BM3D). By validating the effectiveness of unsupervised learning for denoising neutron images, this study establishes a critical first step towards fully AI-driven, end-to-end reconstruction frameworks for ICF diagnostics.

Index Terms—Plasma diagnostics, Image processing, Machine learning, Image filtering, Gaussian noise, Unsupervised Learning, Neutrons, Laser Fusion

I. INTRODUCTION

INERTIAL confinement fusion (ICF) is the process of compressing fusion fuel at high temperature and pressure and allowing inertia to confine the fuel for long enough to induce fusion of atomic nuclei [1,2]. Most commonly, ICF uses deuterium-deuterium (DD) or deuterium-tritium (DT) fusion. It can be designed with direct or indirect drive [3,4]. Direct drive ICF relies on multiple lasers directly heating, ablating and compressing a small capsule containing fusion fuel. In indirect-drive ICF, lasers heat a hohlraum around the capsule, and

radiation from the hohlraum then heats, ablates and compresses the capsule [1,5]. Laser-driven indirect-drive ICF was the method used to achieve scientific breakeven at the Lawrence Livermore National Laboratory's National Ignition Facility (NIF) [1]

A. Neutron Aperture Imaging

Neutron pinhole and penumbral aperture imaging are employed at NIF for measuring the shape of the burning fuel in ICF events [5]. The pinhole apertures are smaller in size than the source while penumbral apertures are larger than the source. To create a larger effective field of view, each NIF neutron imaging system uses an array of apertures that is a mix of pinhole and penumbral apertures.

Due to neutrons' ability to penetrate dense materials, neutron imaging at NIF requires thick apertures. Thus, the images captured are integrations over the source and the translation-variant point-spread function (PSF) of the source. For penumbral apertures, the source information is encoded within the penumbral shadow of the aperture, and image processing and reconstruction techniques are required to determine the source [5]. In contrast, pinhole apertures provide a clearer, more direct image of the source, but for small sources, the images may still require image reconstruction to remove the aperture PSF and make a better estimate of the source.

The image reconstructions at NIF currently use iterative generalized expectation maximization algorithms, which require significant time and frequent human interventions that will be incompatible with any future higher repetition rate ICF facility. An alternative approach for the reconstructions would be to use a fully artificial-intelligence-driven framework.

In this work, we take a first step towards such a framework by investigating using an autoencoder for denoising neutron images from NIF. Such methods would also be directly applicable to denoising many x-ray or gamma-ray images.

B. Image Noise

The NIF images used for this denoising analysis study were captured from image plates that collected neutrons passing through thick pinhole and penumbral apertures, which produces challenges to visual data quality [6]. The low solid angle of pinhole apertures limits their ability to image certain smaller ICF cases appropriately due to decreased signal strength and neutron concentration per pinhole making them more

susceptible to noise than penumbral or annular apertures [5]. Even on high-yield neutron shots, there are numerous sources of noise [4].

Poisson shot noise is produced due to discrete photons or particles colliding with the detector and is most significant in low-yield conditions. Numerous effects can also produce Gaussian noise in the data. Uniform noise, much like Poisson noise, is seen in situations where signals are poor. Salt-and-pepper noise arises during transmission errors or because of sensor defects in camera-based systems, which are also used at NIF. Finally, defects or scratches present on the plate or detector can directly affect the image, causing visible artifacts in those areas.

While there are many noise combinations possible, for the lower-yield shots used in this study, image analysis led to the conclusion that Poisson noise, Gaussian noise, and plate defects are the most common sources of noise to be addressed. After different particle conversions, gain stages, and background subtractions, the noise is closer to Gaussian noise than Poisson or combined Gaussian-Poisson noise in certain NIF images [5]. However, for low-yield shots, Poisson shot noise often combines with Gaussian and is the predominant source of noise in some images [5]. This necessitates extensive work in denoising pinhole images while still retaining the basic properties of the original image, with a specific focus on tackling edge preservation and source reconstruction for NIF data outputs.

C. Image Denoising

Currently, ICF images are usually denoised via filtering methods such as Gaussian filtering, Wiener filtering, and BM3D [7,8]. In recent years, there has been an uptick in the usage of Convolutional Neural Networks (CNNs) to denoise real and simulated neutron pinhole images [9]. While unsupervised methods have been explored more frequently in the recent past due to their small-training-set robustness, they have not been popular for denoising ICF images due to the complex noise environment [10].

The current lack of ground truth data in ICF neutron imaging stems from two main factors. Firstly, there is a relatively limited body of experimental data from NIF, making it difficult to train and test large machine learning models. Additionally, there is a lack of noiseless, clean images that training sets can utilize to learn patterns. Because optimal supervised models must use simulated data conservatively in tandem with real-world data to gain accurate results, this necessitates the development and validation of unsupervised testing methods [8].

Methodologies such as clustering and unsupervised autoencoders can better leverage inherent features of the noisy images rather than relying on potentially inaccurate simulated ground truth datasets during training. Additionally, unsupervised networks require fewer simulated datasets post-tuning, and less validation compared to supervised networks. While unsupervised machine learning methodologies have their own unique challenges with reconstruction error, a combination of an unsupervised method with a filtering method has not been significantly explored as an alternative. A literature search only

yielded one study on this, where a fast Fourier transform was employed as a custom layer in a CNN [11].

This publication explores the use of an unsupervised denoising autoencoder with a discrete CDF 97 wavelet transform in the latent space to denoise and sharpen neutron pinhole images. The CDF 97 biorthogonal wavelet transform has been shown to be highly effective for image denoising due to its excellent energy compaction and smooth basis functions, which enable efficient separation of signal and noise components [12]. Model effectiveness was benchmarked using synthetic ground truth data created by a forward model which was then corrupted by Gaussian and Gaussian-Poisson noise. The noise models produced results representative of experimental NIF data under different neutron yields. The model's performance relative to this synthetically generated ground truth was then compared with a regular autoencoder as a denoising strategy in addition to major filtering methodologies such as BM3D, Gaussian filtering, and Wiener filters; the model was able to outperform ML-only and filtering-only methods for edge preservation metrics such as polar and cartesian coordinate visualization, radial position of the edge, spread of the edge at transitions, residuals, and radial profile. Tikhonov regularization was also applied to evaluate how effectively the reconstruction recovered the original source.

II. MATERIALS AND METHODS

An unsupervised autoencoder with custom layers in the latent space was utilized to denoise pinhole and penumbral data from the NIF dataset. Its performance was assessed using a forward model representing a neutron image. Through the images generated by a basic simulation, the quality of the simulated ground truth was assessed through various edge preservation metrics.

Three classes of datasets were used to validate the functionality of the autoencoder. The first one contained NIF data taken from neutron imaging plates captured by a camera

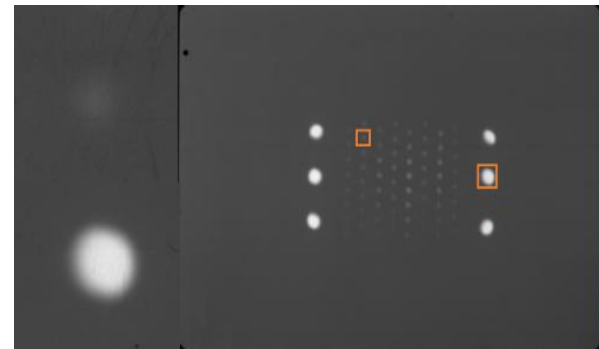


Fig.1. Unprocessed neutron aperture images for NIF shot N210808. Neutrons produced during fusion are uncharged and highly penetrative, allowing them to travel to a scintillator, where they interact and generate visible light. On the left is an example of a pinhole image (top left) and penumbral image (bottom left). Samples for the autoencoder model were taken through region of interest (ROI) extraction of individual penumbras and pinholes.

> REPLACE THIS LINE WITH YOUR MANUSCRIPT ID NUMBER (DOUBLE-CLICK HERE TO EDIT) <

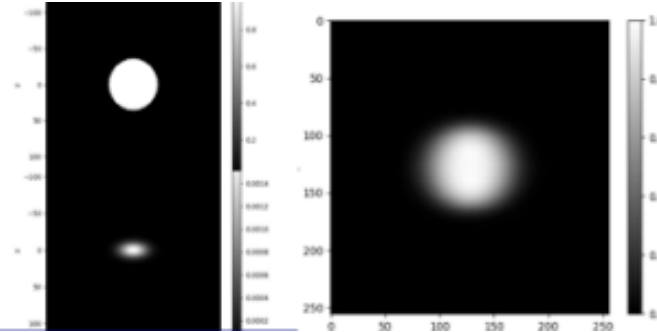


Fig. 2. Illustration of the forward model used for benchmarking. This setup was employed to simulate a penumbral image, which served as the central focus of the study. The simulated pinhole (top left) was convolved with the modeled source distribution (bottom left) to generate a simulated ground truth image of the penumbral aperture (right).

during shots at the facility, while the last two contained data simulated using a forward model following a nonlinear Gaussian and Gaussian-Poisson noise model, respectively. The NIF experimental data was taken from 2 plates captured from shot N210808 as shown in Fig. 1.

Each plate had 64 pinholes each yielding a total available dataset of 128 images. The plate data was then split into smaller regions of interest (ROIs) of size (256, 256) pixels to be passed through the autoencoder as separate datapoints. This dataset was used to prototype the preliminary autoencoder model and served as proof of concept for the feasibility of denoising work using machine learning methods.

The benchmarking datasets used for validating autoencoder functionality were simulated through a forward model that generated a noiseless, simulated ground truth sample of a pinhole or penumbral image. As demonstrated in Fig. 2, the model consisted of two key elements convolved together to produce the simulated ground truth. The Gaussian blur simulates a source image, while the disc represents a pinhole or penumbral aperture depending on its size. To simulate a pinhole, the disc was made to be smaller than the source image. To simulate a penumbral image, the disc was made larger than the source image.

Two datasets representing the noise commonly seen in neutron shots were generated from the forward model. One dataset had exclusively signal-dependent Gaussian noise added to 3000 images, a sample of which is shown at the top of Fig. 3. The noisy image I_n may be expressed as:

$$I_n = I_0 + (RMS(I_0) \times \varepsilon) \quad (1)$$

Here I_0 is the clean image, and ε represents Gaussian noise with a variance of 1.

The other dataset had a combination of Gaussian and Poisson noise as shown in the bottom image of Fig. 3 as follows. The SNR is 10 and ε is Gaussian noise with the same parameters as the previous model:

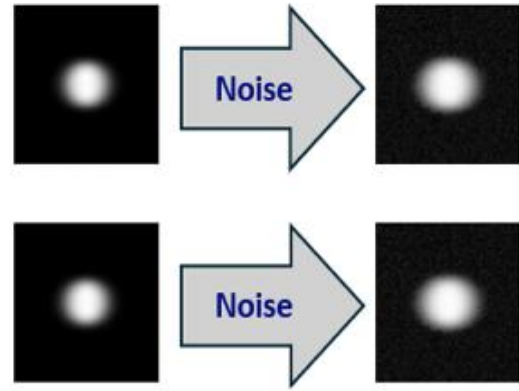


Fig. 3. A sample from the forward model image from Fig. 2a with Gaussian noise (top) and mixed Gaussian-Poisson noise (bottom) added.

$$I_n(x, y) = \text{Poisson}\left(\frac{SNR^2 * I_n(x, y)}{\max(I_n)}\right) \frac{\max(I_0)}{SNR} \quad (2)$$

The autoencoder was built using the PyTorch library and consists of 3 main components: an encoder, a linear transformation layer in the case of penumbral image denoising, a custom CDF 97 discrete wavelet transform layer, and a decoder. As shown in Fig. 4, the image undergoes a series of dimensional transformations as it propagates through the layers of the deep learning model.

The encoder extracts the most relevant features from the inputs by down sampling each image individually. This down sampling process consists of six two-dimensional convolutional layers, each accompanied by leaky ReLU activation function layers that introduce non-linearity during training. This allows the model to learn image features more effectively when compared to linear processes such as Gaussian and Weiner filtering [13].

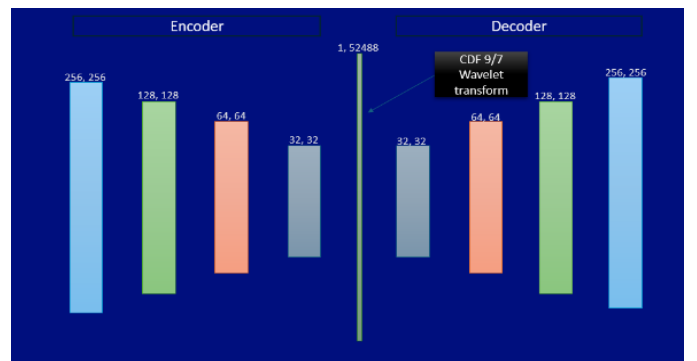


Fig. 4. An illustration of the dimensional transformations applied to each image as it passes through the stages of the autoencoder. The repeated minimization of dimensions within the encoder portion allows for the identification and preservation of key features and the removal of noise vectors. The decoder is then able to reconstruct the denoised image using the most dominant features, while the CDF 97 wavelet transform removes any noise that was missed during the encoding and flattening process.

Meanwhile, the convolutional layers reduce the spatial resolution of the input image by half each time with a kernel size of 5x5, a stride of 2, and a padding value of 2. This combination of kernel size, stride, and padding results in reduction of image dimensions while maintaining the number of feature maps at each layer to ensure that the autoencoder has plenty of information to learn from during instantiation. The first and second convolutional layers were followed by pooling layers after the activation function. The third, fifth, and sixth convolutional and leaky ReLU function pairs were followed by a dropout layer.

The fourth convolutional layer was followed by a dropout layer and pooling layer. Dropout layers were set to 0.2. They were used to help prevent overfitting by randomly zeroing twenty percent of the input units at each layer during each forward pass in the training loop. The pooling layers used had a window size of 2x2 and worked to reduce spatial dimensions even further to ensure that the image was of an appropriate size for the latent space to handle [14].

The encoded transformation is then passed through a custom transformation layer that applies a CDF 97 discrete wavelet transform typically used for preserving image fidelity when compressing JPEG images [15]. In the case of penumbral images, a linear transformation is also applied. Mathematically, the CDF97 transform takes the following general form:

$$\tilde{f} = \text{IDWT}^L(\text{DWT}^L(f)) \approx f \quad (3)$$

L stands for the number of times the transform and its inverse are applied to the image in the latent space. The optimal number of levels was found to be 2, with further levels yielding diminishing returns for results. IDWT refers to the inverse discrete wavelet transform, which is usually applied after performing a discrete wavelet transform (DWT) on an array.

All the synthesis and analysis filter coefficient arrays, $h[n]$, were initialized as 9-tap filters like so:

$$h[n] = \{h_0, h_1, h_2, h_3, h_4, h_5, h_6, h_7, h_8\} \quad (4)$$

However, the analysis high pass and synthesis lowpass filters were padded by zero at the 0th and 8th positions to replicate appropriate CDF97 behavior as described in the original Daubechies publication. The analysis low-pass and synthesis high-pass filters, on the other hand, are not padded and contain all 9 taps like so:

$$\begin{aligned} h[n] &= \{h_0, h_1, h_2, h_3, h_4, h_5, h_6, h_7, h_8\} \\ h[n] &= \{0, h_1, h_2, h_3, h_4, h_5, h_6, h_7, 0\} \end{aligned} \quad (5)$$

This aligns with the boundary handling method described in the original implementation of the CDF 9/7 biorthogonal wavelet filter [12,16]. The numerical values of the nonzero coefficients were derived using the lifting scheme and scaling normalization steps developed by Daubechies [12]. When a linear transformation is needed, the image goes through the following changes in the latent space before being passed to the CDF97 wavelet transform:

$$\begin{aligned} y_{b,c,1,1} &= \frac{1}{H \times W} \sum_{i=1}^H \sum_{j=1}^W x_{b,c,i,j} \\ x_{b,c,1,1} &\rightarrow x_{b,c} \\ z_b &= Wx_b + b \\ y'_b &= W'z_b + b' \end{aligned} \quad (6)$$

These transformations stabilize the variance and reduce the impact of noise in image data. Moreover, the latent space keeps the image vectors (32, 32) in dimension. The feature maps stay constant as well.

After the images are passed through the latent space, the decoder reconstructs the original image from the representation passed to it from the custom layer. It consists of seven convolutional layers. The first two are followed by a batch normalization and leaky ReLU layer. The third and fourth layers are only superseded by leaky ReLU activation functions. To prevent checkerboarding in the image background during reconstruction, the last three layers are preceded by up-sampling layers in bicubic mode. Each time, the image is up-sampled by a factor of 2 using bicubic interpolation, which doubles the spatial dimensions at each step and reverses the down-sampling done by the encoder. While the first five activation layers are ReLU functions, the activation function of the last layer is a Sigmoid outputting values between 0 and 1. This makes it optimal for reconstructing and working with grayscale images that typically have pixel values between 0 and 1.

The images were run through the autoencoder for 30 epochs. The learning rate was 0.001 and data indices were shuffled each epoch. A batch size of 10% of the sample size was found to be the most optimal for reconstruction. Hence, for the simulated ground truth data used for benchmarking, the batch size was set to be 300 and for the NIF data, the batch size was set to be 12. A smooth variant of the L1 loss, known as Smooth L1 or Huber loss, was used as the loss function. It behaves quadratically for small errors and linearly for large errors, reducing sensitivity to outliers while maintaining differentiability [17]. Smooth L1 Loss can be expressed mathematically like so:

$$L(x) = \begin{cases} 0.5(x - y)^2 & \text{if } |x - y| \leq 0 \\ |x - y| & \text{if } |x - y| > 0 \end{cases} \quad (7)$$

was used in lieu of Mean Squared Error due to its resilience to outliers and frequent use in image denoising and dehazing algorithms [18]. Additionally, when reconstruction error was compared, the model performed better with Smooth L1 Loss as opposed to MSE for the given datasets.

III. RESULTS

Both the synthetic ground truth and NIF datasets were utilized to generate and analyze results. These datasets objectively assessed the autoencoder's ability to denoise mixed Gaussian-Poisson noise under the physics constraints imposed upon the system by the forward model. The NIF dataset was used as proof of concept to ascertain that a basic autoencoder could perform generalizable denoising in practical, noisy conditions that reflect true experimental variability and Gaussian-Poisson

> REPLACE THIS LINE WITH YOUR MANUSCRIPT ID NUMBER (DOUBLE-CLICK HERE TO EDIT) <

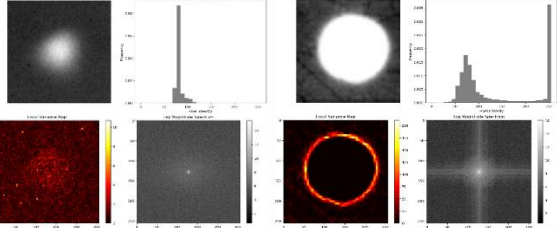


Fig. 5. To confirm the type of noise present in the images, a histogram, local variance plot, and power spectra were generated for a pinhole and penumbral image from the N210808 shot. The noise was ascertained to be mixed Gaussian and Poisson across the images due to the features and characteristics of the plots.

characteristics within NIF datasets. The denoised, reconstructed results from the autoencoder were compared to datasets denoised with BM3D, a widely regarded benchmark method in image denoising [19]. For each method, the denoised reconstructions were compared to the ground truth. Assessment metrics included visual polar and cartesian coordinate visualization, radial position of the edge, spread of the edge at transitions, residuals, and radial profile. Tikhonov regularization, also known as ridge regression, was also applied along with Weiner deconvolution to evaluate how effectively the reconstruction recovered the original source when compared to the ground truth.

To create a reliable denoising solution for the images at hand, it was essential to validate that the noise present in the NIF data was indeed mixed Gaussian-Poisson in nature [5]. As an alternative, histogram analysis, local variance analysis, and power spectrum analysis as displayed in Fig. 5 were employed to acquire more information about the nature of the noise present in the data [20].

The results of these analyses for both pinhole and penumbral images indicate mixed Gaussian-Poisson noise. Pixel intensity histograms of NIF data are slightly skewed left with a bell-curve shape in both cases. This shape suggests the presence of Gaussian noise, while the skew indicates that Poisson noise may also contribute to visual distortions in the image [20]. In the case of the pinhole image, the local variance map displays higher variance in lighter areas of the image when compared to darker areas. A similar trend is seen at the edges of the penumbral image. Poisson noise in low-light conditions is often characterized as greater in magnitude at higher pixel intensities; hence, increased variance at higher pixel intensities in both images is an indicator of this type of noise [21]. In the case of the pinhole image, Fourier spectrum analysis results in a grainy background with poorly defined frequency and phase components. The background indicates that the image contains high levels of Gaussian noise, while the lack of frequency and phase bands in the case of the pinhole aperture indicate the presence of Poisson noise as well due to its signal dependent nature [22,23]. The pinhole, on the other hand, displays strong frequency and phase components against a grainy background. This indicates that while Poisson noise may not be as significant a problem in penumbral images, Gaussian noise is still pervasive throughout this portion of the image.

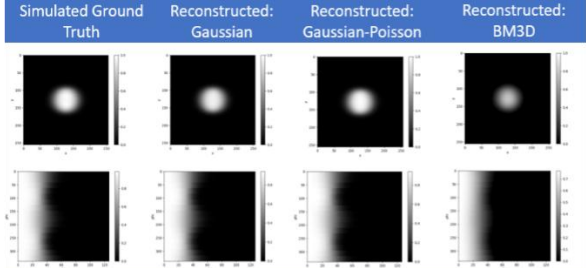


Fig. 6. The simulated ground truth visualized side-by-side with autoencoder reconstructions of images corrupted by Gaussian noise and Gaussian-Poisson noise. For comparison, the BM3D method was utilized to reconstruct an image with Gaussian-Poisson noise and can be seen on the right. Both cartesian (top) and polar (bottom) results indicate higher fidelity between the ground truth and autoencoder reconstructions than compared to the ground truth and BM3D reconstruction.

Reconstruction error measures the discrepancy between an autoencoder's input and its reconstructed output, often quantified using pixel-wise losses and structural similarity metrics. During training, the model's weights and biases are iteratively updated to minimize this error [24]. A viable autoencoder, in reconstructing noisy data, must be able to produce a result that matches the original ground truth image the inputs are derived from as closely as possible. While the most common method for assessing reconstruction fidelity is Mean Squared Error (MSE), other values such as Peak Signal to Noise Ratio, Structural Similarity Index, and edge preservation metrics [24,25]. Since the most significant aspect of reconstruction for neutron imaging is edge preservation and source reconstruction, most of the results are focused on this. Visual polar and cartesian coordinate visualization, radial position of the edge, spread of the edge at transitions, residuals, and radial profile were all considered. Additionally, Tikhonov regularization was also applied to evaluate how effectively the reconstruction recovered the original source.

Fig. 6 displays a polar and cartesian visualization of the reconstructions indicated high fidelity between the ground truth and the denoised images. Key structural features and spatial patterns were preserved across both representations, indicating that the denoising process maintained the essential image characteristics without introducing noticeable artifacts. The alignment between the ground truth and denoised images was particularly evident in the preservation of the Gaussian blur along the edges. This suggests that the autoencoder effectively distinguishes between the blur inherent to the ground truth and extraneous noise introduced during noise generation in both the Gaussian and Gaussian-Poisson experimental cases. This selective retention further supports the qualitative accuracy of the reconstruction.

Fig. 7 illustrates a quantitative analysis of the radius as a function of degree in the simulated ground truth, compared to autoencoder-based reconstructions under Gaussian and Gaussian-Poisson noise models, demonstrated performance on par with established denoising techniques such as BM3D. In

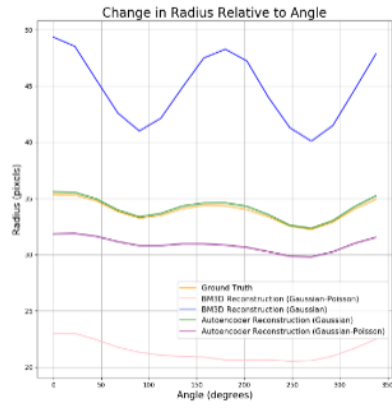


Fig. 7. Change in radius relative to angle for reconstructed images. Ground truth is compared to autoencoder and BM3D.

images corrupted by Gaussian noise, the autoencoder reconstructions exhibited near-perfect agreement with the ground truth, accurately recovering the underlying magnitude of the radial profile. In the presence of Gaussian-Poisson noise, the reconstructions displayed a marginal reduction in estimated radius of approximately four pixels but effectively preserved the overall radial trend consistent with the simulated ground truth. To further compare edge fidelity across differing denoising methods and noise models, the absolute radius error is defined as:

$$\varepsilon_r = |\hat{r} - r_{GT}| \quad (8)$$

and relative fidelity scores were computed using:

$$Fidelity_{AE \text{ vs. } BM3D} = \left(1 - \frac{\varepsilon_r^{AE}}{\varepsilon_r^{BM3D}} \right) \times 100 \quad (9)$$

For samples corrupted by Gaussian noise, the autoencoder reconstructions showed a mean absolute radius error of ____ pixels, outperforming BM3D's ____ pixels. The relative fidelity scores were computed to be ____ % and ____ %, respectively.

For samples corrupted by Gaussian-Poisson noise, autoencoder reconstructions showed a mean absolute radius error of ____ pixels, while BM3D reconstructions had an error of ____ pixels. For these sample sets, the relative fidelity scores were ____ % for autoencoder reconstructions and ____ % for BM3D reconstructions. Additionally, the Pearson correlation coefficient was computed for radial profiles to assess structural fidelity. Under Gaussian noise, the autoencoder achieved a correlation of ____, slightly higher than BM3D's _____. Under Gaussian-Poisson noise, all methods exhibited decreased correlation of ____, with the autoencoder maintaining strong agreement around _____. These results demonstrate that the autoencoder preserves radial structure with high accuracy under both noise models and performs competitively with traditional denoising methods, particularly in terms of structural and metric fidelity.

Fig. 8 shows a visualization of the Gaussian blur variance,

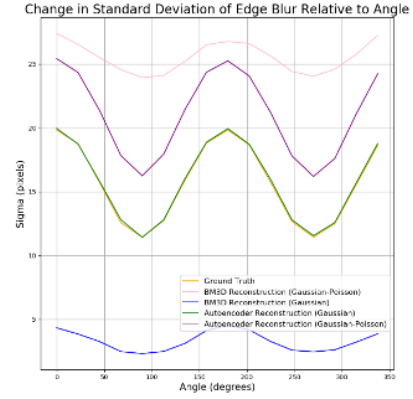


Fig. 8. Change in standard deviation of image edge blur in pixels relative to angle. Ground truth is compared to autoencoder and BM3D reconstructions graphically.

also known as σ at edge transitions in the reconstructions exhibited high fidelity to the ground truth in images degraded by Gaussian noise, accurately preserving edge sharpness and gradient continuity. This is supported by a high edge PSNR of 34.2 dB and a low gradient magnitude similarity deviation (GMSD) of 0.078. Under Gaussian-Poisson noise, the reconstructions exhibited elevated variance levels, reflecting the autoencoder's increased difficulty in disentangling structured blur from unnecessary noise under more complex noise conditions. This is supported by an elevated local gradient variance at the edges, rising from ____ to _____. Despite this challenge, the reconstructions maintained the expected σ -blur trend, albeit at a higher variance overall. Autoencoder-based methods outperformed BM3D in preserving the integrity of the σ profile in both Gaussian and Gaussian-Poisson noise situations, demonstrating superior retention of spatially dependent blur characteristics when compared to conventional filtering methods. Specifically, the mean squared error (MSE) between the reconstructed and ground truth σ -blur profiles was ____ for the autoencoder, compared to ____ for BM3D, indicating significantly improved spatial fidelity in blur retention. Additionally, edge PSNR and GMSD scores consistently favored the autoencoder, underscoring its superior

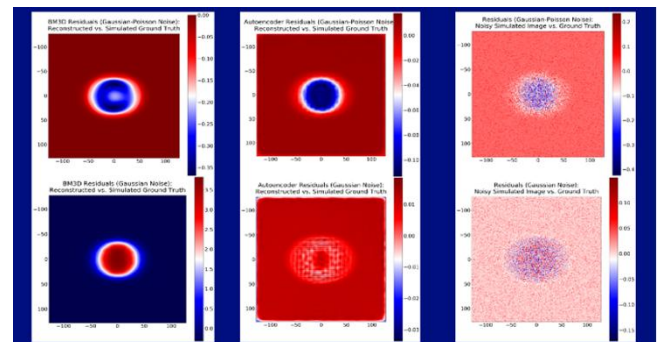


Fig. 9. Residual analysis of reconstructions relative to the ground truth indicates high fidelity in the presence of Gaussian noise. Autoencoder reconstructions outperformed BM3D reconstructions in the presence of mixed Gaussian-Poisson noise.

ability to preserve spatially dependent blur characteristics compared to conventional filtering approaches.

Fig. 9 displays residual analysis of the reconstructions relative to the ground truth. It demonstrated high fidelity in the presence of Gaussian noise. Residuals in this case were tightly distributed, with a mean of 0.012, a median of 0.011, and a standard deviation of 0.005. Residual values were consistently constrained within the range [0.00, 0.03] across the image domain. For images affected by Gaussian-Poisson noise, residuals were notably higher and more dispersed, with a mean of 0.041, a median of 0.038, and a standard deviation of 0.018. They generally ranged between [0.00, 0.10], reflecting the increased complexity in accurately reconstructing pixel intensities under mixed noise conditions. However, the autoencoder was able to reduce residuals of the reconstructions by 71.4% on average in the case of images corrupted by Gaussian-Poisson noise and by 70.0% on average in the case of images corrupted by Gaussian noise alone. This is an improvement when compared to BM3D, which only reduces residuals by ____% on average in the case of images with Gaussian-Poisson noise and ____% in the case of images with Gaussian noise alone. In the case of BM3D, the average residual values of 0.059 (mean), 0.055 (median), and 0.022 (standard deviation) under Gaussian-Poisson noise, and 0.021 (mean), 0.020 (median), and 0.007 (standard deviation) for Gaussian noise demonstrate the autoencoder's improved denoising capability when compared to BM3D in the presence of complex, nonlinear noise.

As shown in Fig. 10, radial profile analysis of the autoencoder reconstructions relative to the simulated ground truth revealed that, under Gaussian-Poisson noise, the reconstructed pixel intensities were initially attenuated, with values starting around 0.8 compared to the ground truth peak of 1.0. However, as the radius increased, the profile gradually converged toward the ground truth, indicating that the reconstruction effectively recovered the overall structure despite initial underestimation. In contrast, reconstructions from Gaussian noise exhibited near-perfect alignment with the ground truth across the entire radial domain, demonstrating the autoencoder's high fidelity under simpler noise conditions.

To validate the fidelity of the reconstructions further, the source image was recovered from both the ground truth and reconstructed outputs using Wiener deconvolution in conjunction with Tikhonov regularization, incorporating the known point spread function (PSF) of the forward model defined as the sum of the initial disc before convolution with

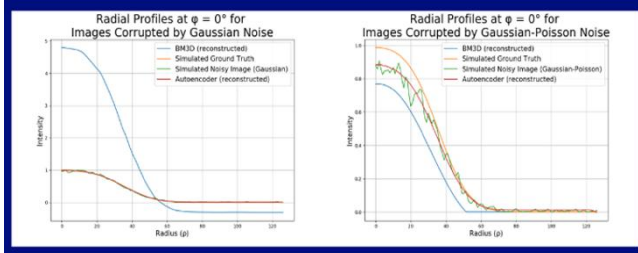


Fig. 10. Radial profile analysis

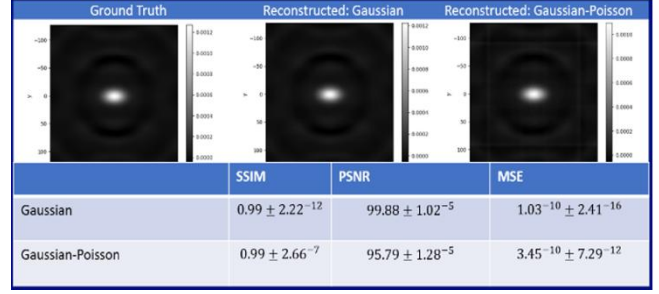


Fig. 11. Tikhonov regularization

the source of the forward model. In both the Gaussian and Gaussian-Poisson noise scenarios, the deconvolved reconstructions closely approximated the true source, demonstrating the autoencoder's ability to preserve critical sources spatial information through the noise. The recovered exhibited high structural similarity to the ground truth, further validating the effectiveness of the reconstruction pipeline under varying noise conditions.

Fig. 11 shows a visualization of the results relative to the ground truth along with structural similarity, peak signal to noise ratios, and mean squared error values. After training and validating the autoencoder using simulated ground truth data, the model was applied to NIF pinhole and penumbral images. Fig. 12 displays the results of running the autoencoder on 50 pinhole images and 6 penumbral images with a batch size of 6 and 2, respectively. The reconstructions exhibited strong qualitative and quantitative agreement with expected structural features, indicating that the autoencoder successfully generalized from simulated to real-world conditions. This demonstrates the model's robustness and practical applicability in processing experimental data following tuning on synthetic datasets.

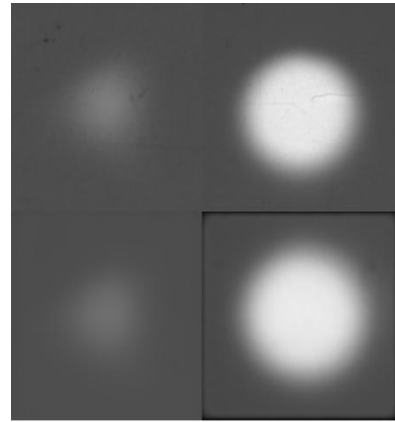


Fig. 12: Denoised NIF pinhole (left column) and penumbral images (right column), respectively. These results were achieved with the benchmarked autoencoder on a limited amount of training data. They indicate that the model has consistent reconstruction capability in real-world scenarios where thousands of data points may not be accessible.

IV. DISCUSSION

Our unsupervised autoencoder approach demonstrates clear advantages over conventional denoising methods for neutron images corrupted by Gaussian noise, particularly in edge preservation. For images affected by Gaussian-Poisson noise, the model achieved performance comparable to established methods such as BM3D and Wiener filtering. These results indicate that unsupervised learning can match or exceed traditional approaches while eliminating the need for external training datasets, learning instead directly from the intrinsic features of noisy input data.

These results offer unsupervised learning as a powerful tool in denoising neutron imaging data for ICF research. The autoencoder framework presented here not only eliminates the need for large, labeled datasets but also reduces the complexity of preprocessing pipelines, such as multi-step transformations often used for Gaussian-Poisson denoising. This reduction in complexity is particularly valuable in high-throughput environments like the National Ignition Facility, where real-time or near-real-time image processing is advantageous for adjusting experimental parameters on the fly.

Additionally, the incorporation of a CDF 97 wavelet transform in the autoencoder's latent space enhances sensitivity to fine-grained features across multiple scales, enabling better detection of subtle spatial patterns and edge information in neutron source distributions. The wavelet-based representation complements the autoencoder's ability to generalize, providing more robust encoding of structural features that conventional filtering methods tend to degrade.

While this framework represents an initial step toward AI-based image reconstruction for ICF diagnostics, it has immediate practical applications. The method is directly applicable to pinhole imaging that does not require image reconstruction to remove the PSF of the aperture, such as some x-ray pinhole imaging. More broadly, it establishes a foundation for future developments in rapid source-distribution reconstruction from neutron imaging data, a challenging inverse problem.

V. CONCLUSION

This study demonstrates the effectiveness of an unsupervised autoencoder with custom and convolutional layers for the denoising of NIF ICF pinhole images. This method outperforms widely used filtering methods (BM3D, Wiener filtering, and Gaussian filtering) in minimizing reconstruction error while maximizing edge preservation. Unlike supervised machine learning denoising approaches that require extensive training set data, which is often simulated due to a lack of ground truth data, this unsupervised method relies on features extracted directly from each input image, reducing dependence on external data beyond initial validation. This adaptability is particularly valuable for ICF imaging, where many images are taken in low-yield, low-shot-rate conditions that preclude obtaining ground truth or large real-data training sets. The custom layer in the bottleneck of the autoencoder contributes measurably to improved denoising performance when compared to baseline models without it.

Despite these advantages, several limitations must be addressed to establish the algorithms utility. The model has been validated primarily on neutron images from smaller segments of the imaging plate rather than on the full data set, and its generalizability to other image types, e.g. x-ray images, or less common source shapes and apertures configurations. Additionally, unsupervised approach struggles to fully resolve nonlinearities introduced by compound noise distributions, such as overlapping Poisson-Gaussian processes. Quantifying potential overfitting and defining clear operational boundaries will be essential for reliable use.

Future work should explore physics-informed loss functions and hybrid models that combine unsupervised and semi-supervised paradigms to improve noise-specific adaptability. Domain-specific augmentations and simulation-based priors may further enhance performance in low-signal or anisotropic imaging scenarios typical of early-stage ICF implosions.

Ultimately, this study reinforces the potential of unsupervised machine learning for neutron image enhancement and establishes a foundation for a broader class of self-tuning algorithms for ICF diagnostics. By bridging the gap between traditional filtering approaches and data-intensive supervised learning, this methodology offers a scalable, generalizable framework for fusion research applications, from time-series denoising and 3D tomographic reconstruction to anomaly detection in neutron yield patterns.

REFERENCES

- [1] O. Hurricane, P. Patel, R. Betti, D. Froula, S. Regan, S. Slutz, M. Gomez, and M. Sweeny, "Physics principles of inertial confinement fusion and U.S. program overview," *Reviews of Modern Physics*, vol. 95, Jun. 2023, doi: <https://doi.org/10.1103/RevModPhys.95.025005>
- [2] D. Keefe, "Inertial Confinement Fusion," *Lawrence Berkeley National Laboratory*, LBNL Report #: LBL-14194, Mar. 1982.
- [3] Z. Lu, S. Jia, G. Li, and S. Jing, "Neutron image denoising method based on adaptive new wavelet threshold function," *Nuclear Instruments and Methods in Physics Research Section A Accelerators Spectrometers Detectors and Associated Equipment*, vol. 1059, pp. 169006–169006, Dec. 2023, doi: <https://doi.org/10.1016/j.nima.2023.169006>.
- [4] Naima Naheed, B. T. Wolfe, and Z. Wang, "Noise classification of ICF images using a convolutional neural network (CNN)," *Zenodo (CERN European Organization for Nuclear Research)*, Aug. 2023, doi: <https://doi.org/10.5281/zenodo.8368998>.
- [5] D. N. Fittinghoff, N. Birge, and V. Geppert-Kleinrath, "Neutron imaging of inertial confinement fusion implosions," *Review of Scientific Instruments*, vol. 94, no. 2, Feb. 2023, doi: <https://doi.org/10.1063/5.0124074>.
- [6] H. Feng, L. Wang, X. Wang, and J. Jin, "Ultrasonic manipulation for precise positioning and equidistant transfer of inertial confinement fusion microspheres," *Ultrasonics*, vol. 126, p. 106806, Dec. 2022, doi: <https://doi.org/10.1016/j.ultras.2022.106806>.
- [7] B. T. Wolfe, P. Chu, N. Nguyen-Fotiadis, X. Zhang, M. A. Alvarez, and Z. Wang, "Machine learning-driven image synthesis and analysis applications for inertial confinement fusion (invited)," *Review of Scientific Instruments*, vol. 95, no. 12, Dec. 2024, doi: <https://doi.org/10.1063/5.0219412>.
- [8] Y. Xiaohui *et al.*, "Image restoration method suitable for neutron imaging system image and based on Gauss-Poisson hybrid noise model," *European Patent Office*.
- [9] Z. Lu *et al.*, "Neutron radiographic images denoising method based on multi-branch network," *Nuclear Instruments and Methods in Physics Research Section B Beam Interactions with Materials and Atoms*, vol. 553, pp. 165402–165402, May 2024, doi: <https://doi.org/10.1016/j.nimb.2024.165402>.

> REPLACE THIS LINE WITH YOUR MANUSCRIPT ID NUMBER (DOUBLE-CLICK HERE TO EDIT) <

- [10] X. Lin, C. Ren, X. Liu, J. Huang, and Y. Lei, "Unsupervised Image Denoising in Real-World Scenarios via Self-Collaboration Parallel Generative Adversarial Branches," *2021 IEEE/CVF International Conference on Computer Vision (ICCV)*, pp. 12608–12618, Oct. 2023, doi: <https://doi.org/10.1109/iccv51070.2023.01162>.
- [11] X. Li *et al.*, "FEUSNet: Fourier Embedded U-Shaped Network for Image Denoising," *Entropy*, vol. 25, no. 10, pp. 1418–1418, Oct. 2023, doi: <https://doi.org/10.3390/e25101418>.
- [12] I. Daubechies and Wim Sweldens, "Factoring wavelet transforms into lifting steps," *Journal of Fourier Analysis and Applications*, vol. 4, no. 3, pp. 247–269, May 1998, doi: <https://doi.org/10.1007/bf02476026>.
- [13] N. Kulathunga *et al.*, "Effects of the Nonlinearity in Activation Functions on the Performance of Deep Learning Models," doi: <https://doi.org/10.48550/arXiv.2010.07359>
- [14] A. Krizhevsky, I. Sutskever, and G. E. Hinton, "ImageNet Classification with Deep Convolutional Neural Networks," *Communications of the ACM*, vol. 60, no. 6, pp. 84–90, May 2012.
- [15] J. Mishra and V. Kumar, "Study of Digital Image Compression Techniques and Framework for Suitability Selection based on Similarity Measuring Metrics," *2022 13th International Conference on Computing Communication and Networking Technologies (ICCCNT)*, pp. 1–6, Jun. 2024, doi: <https://doi.org/10.1109/icccnt61001.2024.10724007>.
- [16] J. Park, D. Kwon, Y. Song, and C. Ahn, "A Study on Feature Extraction of Transformers Aging Signal using Discrete Wavelet Transform Technique," *Proceedings of the Korean Institute of Electrical and Electronic Material Engineers Conference*, pp. 5-12, May. 2000.
- [17] C. Liu *et al.*, "Adaptive Smooth L1 Loss: A Better Way to Regress Scene Texts with Extreme Aspect Ratios," *2021 IEEE Symposium on Computers and Communications (ISCC)*, Sep. 2021, doi: <https://doi.org/10.1109/iscc53001.2021.9631466>.
- [18] Zhu, Xinshan *et al.*, "Multi-Stream Fusion Network With Generalized Smooth L1 Loss for Single Image Dehazing," *IEEE transactions on image processing* 30 (2021): 7620–7635. Print.
- [19] Ahmed, A. M. Jawad, S. A. Abdulkareem, F. M. Mustafa, Svitlana Ivanchenko, and Serhii Toliupa, "BM3D Denoising Algorithms for Medical Image," *DOAJ (DOAJ: Directory of Open Access Journals)*, pp. 135–141, Apr. 2024, doi: <https://doi.org/10.23919/fruct61870.2024.10516419>.
- [20] S. Akbar and A. Verma, "Analyzing Noise Models and Advanced Filtering Algorithms for Image Enhancement."
- [21] K. G. Lore, A. Akintayo, and S. Sarkar, "LLNet: A deep autoencoder approach to natural low-light image enhancement," *Pattern Recognition*, vol. 61, pp. 650–662, Jan. 2017, doi: <https://doi.org/10.1016/j.patcog.2016.06.008>.
- [22] T. Le, R. Chartrand, and T. J. Asaki, "A Variational Approach to Reconstructing Images Corrupted by Poisson Noise," *Journal of Mathematical Imaging and Vision*, vol. 27, no. 3, pp. 257–263, Mar. 2007, doi: <https://doi.org/10.1007/s10851-007-0652-y>.
- [23] A. Faramarzi, A. Ahmadyfard, and H. Khosravi, "Adaptive Image Super-Resolution Algorithm Based on Fractional Fourier Transform," *Image Analysis & Stereology*, vol. 41, no. 2, pp. 133–144, Jul. 2022, doi: <https://doi.org/10.566/ias.2719>.
- [24] F. Zhuang, Supervised Representation Learning: Transfer Learning with Deep Autoencoders
- [25] L. Gondara, "Medical Image Denoising Using Convolutional Denoising Autoencoders," *IEEE Xplore*, 2016. <https://ieeexplore.ieee.org/abstract/document/7836672/>
- [26] A. Bijaoui, E. Slezak, "Analysis of radial profiles," Jan. 1987.
- [27] C. Zucker and H. H.-H. Chen, "RadFil: A Python Package for Building and Fitting Radial Profiles for Interstellar Filaments," *The Astrophysical Journal*, vol. 864, no. 2, p. 152, Sep. 2018, doi: <https://doi.org/10.3847/1538-4357/aad3b5>.
- [28] E. Mavridaki and V. Mezaris, "NO-REFERENCE BLUR ASSESSMENT IN NATURAL IMAGES USING FOURIER TRANSFORM AND SPATIAL PYRAMIDS," in *IEEE Proceedings*, IEEE, Oct. 2014.